Measurements of magneto-Rayleigh–Taylor instability growth during the implosion of initially solid metal liners[a)]

D. B. Sinars,[1,b)] S. A. Slutz,[1] M. C. Herrmann,[1] R. D. McBride,[1] M. E. Cuneo,[1] C. A. Jennings,[1] J. P. Chittenden,[2] A. L. Velikovich,[3] K. J. Peterson,[1] R. A. Vesey,[1] C. Nakhleh,[1] E. M. Waisman,[1] B. E. Blue,[4] K. Killebrew,[4] D. Schroen,[4] K. Tomlinson,[4] A. D. Edens,[1] M. R. Lopez,[1] I. C. Smith,[1] J. Shores,[1] V. Bigman,[1] G. R. Bennett,[1] B. W. Atherton,[1] M. Savage,[1] W. A. Stygar,[1] G. T. Leifeste,[1] and J. L. Porter[1]
[1]*Sandia National Laboratories, P.O. Box 5800, Albuquerque, New Mexico 87185, USA*
[2]*Blackett Laboratory, Imperial College, London SW7 2BW, United Kingdom*
[3]*Plasma Physics Division, Naval Research Laboratory, Washington, D.C. 20375, USA*
[4]*General Atomics, San Diego, California 92121, USA*

(Received 19 November 2010; accepted 20 December 2010; published online 7 April 2011)

A recent publication [D. B. Sinars *et al.*, Phys. Rev. Lett. **105**, 185001 (2010)] describes the first controlled experiments measuring the growth of the magneto-Rayleigh–Taylor instability in fast (~100 ns) Z-pinch plasmas formed from initially solid aluminum tubes (liners). Sinusoidal perturbations on the surface of these liners with wavelengths of 25–400 μm were used to seed single-mode instabilities. The evolution of the outer liner surface was captured using multiframe 6.151 keV radiography. The initial paper shows that there is good agreement between the data and 2-D radiation magneto-hydrodynamic simulations down to 50 μm wavelengths. This paper extends the previous one by providing more detailed radiography images, detailed target characterization data, a more accurate comparison to analytic models for the amplitude growth, the first data from a beryllium liner, and comparisons between the data and 3D simulations. © *2011 American Institute of Physics*. [doi:10.1063/1.3560911]

I. INTRODUCTION

This paper extends a previous publication describing the first controlled measurements of the magneto-Rayleigh–Taylor (MRT) instability in fast (~100 ns) Z-pinches.[1] The MRT instability[2–5] is ubiquitous to pinch plasmas in which the $J \times B$ force is used to compress matter. In these experiments the Z-pinch plasma was formed from an initially solid metal tube commonly referred to as a liner. A linearly rising current pulse is applied along the liner's axis (the z-axis) with a rise time of 100 ns and a peak current of about 20 MA, which creates a radially inward $J \times B$ force on the liner and turns it into plasma. In cylindrical liner implosions the MRT instability arises at the outer plasma–vacuum interface, where the driving magnetic pressure plays a role analogous to a light fluid pushing on a heavy fluid (the plasma liner) as in the classical fluid Rayleigh–Taylor instability. The MRT instability is more complex in part because the driving current is not confined to the surface boundary but diffuses into the liner, allowing resistive heating of the liner and distributing the magnetic pressure. The effect of the instability is to break up the integrity of the imploding cylindrical plasma so that it does not reach its axis in an intact state. Thus, the MRT instability can negatively impact all applications of fast Z-pinches.

An application of immediate interest is direct-drive inertial confinement fusion in which a cylindrical liner containing fuel (deuterium and/or tritium) is compressed by the magnetic pressure to the conditions needed to produce fusion yield.[6,7] It is thought that it may be possible to achieve significant fusion yield on the 26 MA Z facility (>100 kJ) if adequate compression of the fuel can be obtained (R_0/R_{final} =20–30). The major factor limiting the integrity of the liner and our ability to compress the fuel is the breakup of the liner due to the MRT instability. Design calculations suggest that the impact of the MRT instability can be mitigated by the use of relatively thick liners, so that the instability growing up on the outside liner surface does not disrupt the inside liner surface enough to significantly degrade the yield. Some example calculations of such a liner are shown in Fig. 1. Given the complexity of the multiphysics simulation tools used to make these design calculations, experimental data to benchmark the calculations are needed.

There are surprisingly few experiments studying the growth of the MRT instability in the literature. The only submicrosecond data we found is from wire-array tests using wires with axial modulations in the initial mass per unit length.[8] Liners composed of an azimuthally continuous, cylindrical tube initiate and evolve differently than liners composed of individual 5–30 μm diameter wires spaced 0.2–2 mm apart azimuthally. Wire-array implosions are dominated by the ablation of about half the initial mass into the array interior before the implosion begins, a consequence of the large skin depth of the current and the small diameter of the wires.[9–11] By contrast, the thickness of the cylindrical tube liners proposed for magnetized liner inertial fusion[6] exceeds the skin depth of the proposed current pulse, and no significant prefilling of the interior volume is expected. The remaining published controlled studies of MRT growth were

[a)]Paper UI3 3, Bull. Am. Phys. Soc. **55**, 332 (2010).
[b)]Invited speaker.

 © 2011 American Institute of Physics

Downloaded 04 May 2011 to 198.102.153.2. Redistribution subject to AIP license or copyright; see http://pop.aip.org/about/rights_and_permissions

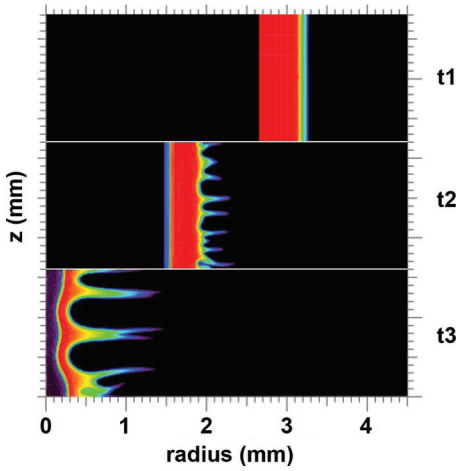

FIG. 1. (Color) Color-coded density contours from a 2D simulation of a beryllium liner near the start of the current pulse (t1), midway (t2), and close to stagnation on axis (t3). The liner has an initial outer radius to thickness ratio of 6 and a 60 nm surface roughness amplitude. Though prominent bubble-spike structures develop due to the magneto-Rayleigh–Taylor instability, the inside liner surface remains intact enough to compress fusion fuel to obtain about 86% of the 1D simulated yield (Ref. 6).

done on multimicrosecond generators in which the imploding liners have significant material strength and remain in liquid or solid states for much of the implosion.[12] By contrast, in fast (~100 ns) implosions strong shocks can develop in the liner and the liner is typically in the plasma state for much of the implosion. Due to the lack of high-quality data for the submicrosecond regime, the magnetohydrodynamics physics packages of simulation codes (e.g., LASNEX,[13] HYDRA,[14] GORGON[15]) are not well validated. The need for high-quality data for validation purposes is reflected in the fact that each of these codes initially gave differing predictions for our experiments.

The remainder of this paper describes the experimental configuration, target characterization data, radiography data obtained on the MRT instability development, and comparisons to theory and simulations. Plans and prospects for future integrated inertial confinement fusion tests are discussed in the summary.

II. EXPERIMENTAL SETUP

In this paper we present data from three series of controlled MRT growth experiments on the 26 MA, 100 ns Z facility in which radiography was used to quantify the growth of the instability. The hardware configuration and current drive for these experiments are summarized in Fig. 2 and Fig. 3, respectively. The power feed design shown in Fig. 2(a) was designed to minimize current loss in the feed based on insights from comparisons of different feed geometries (e.g., Fig. 13 of Ref. 16). The feed design shown was optimized for minimal inductance using the techniques of Ref. 17 with the constraints that we wanted electrode contours with continuous first and second derivatives and large radii of curvature. The currents were measured with 4–5 B-dot monitors placed in the anode at the entrance to the power feed.[18] Cylindrical tubelike liners made of Al 1100 alloy or beryllium were placed inside of an 8 post, 26 mm inner diameter return-current structure (can). The Al liners had an

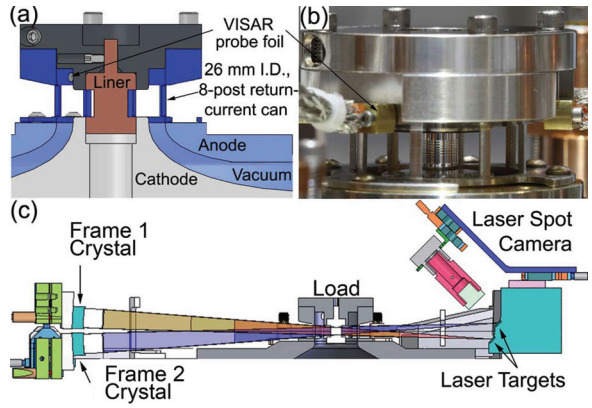

FIG. 2. (Color) Description of the hardware used during the experiments. (a) Half-section diagram of the power-feed hardware surrounding the load. (b) Photograph of the return-current can and liner as installed in the Z facility. (c) Schematic of the two-frame backlighter illustrating the 3° angle above/below horizontal. In the one-frame system only a single laser target and crystal are used, which are all positioned to lie in the horizontal plane passing through the midheight of the target.

outer radius of 3.168 mm, a wall thickness of 292 μm, and contained a 2 mm diameter tungsten rod on the liner axis. The Be liners had an outer radius of 3.19 mm, a wall thickness of 813 μm, and also contained a 2 mm diameter tungsten rod on the axis. The large return-current can radius was chosen to reduce the azimuthal variations in the static magnetic field caused by the eight posts to <1%. The rod was used to quench radiation produced by the plasma stagnation on axis. The liner dimensions are similar to those being considered for future magnetized liner inertial fusion experiments.[6]

The MRT instability was seeded in the aluminum liner experiments by machining sinusoidal perturbations with peak-to-valley amplitudes that were 5% of the wavelength. In the first set of experiments, the liners used wavelengths with $\lambda = 200$ and 400 μm (10, 20 μm peak-to-valley amplitudes, respectively). The instability growth was recorded at eight different times during the implosion using two-frame, monochromatic 6.151 keV backlighting.[19] A second set of Al experiments used targets with wavelengths of 25, 50, 100, and 200 μm and a large flat region in the backlighter field of view. A one-frame 6.151 keV diagnostic[20] was used to provide a horizontal (0°) view to prevent shadowing of the

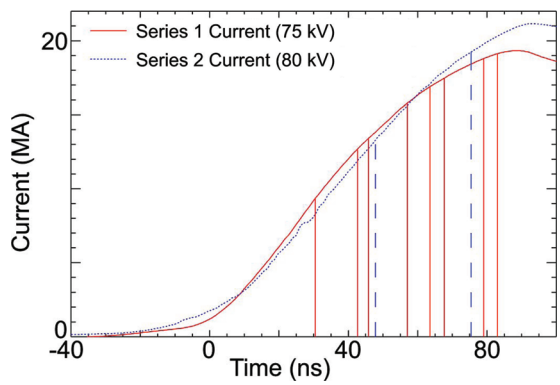

FIG. 3. (Color) Measured load currents from the Al target experiments. The radiograph times are overlaid as vertical bars. Slightly different machine configurations were used during the two experimental series, resulting in a slightly higher peak current and larger foot during series 2.

Downloaded 04 May 2011 to 198.102.153.2. Redistribution subject to AIP license or copyright; see http://pop.aip.org/about/rights_and_permissions

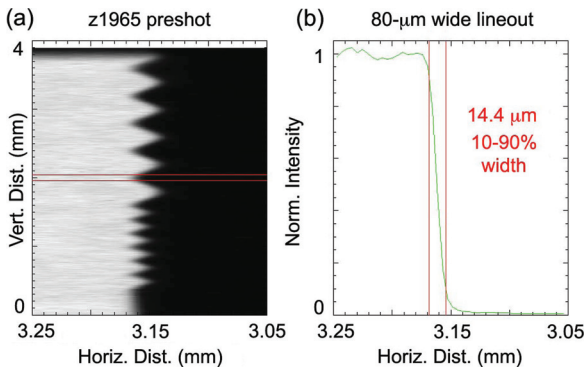

FIG. 4. (Color) Analysis of a preshot radiograph from z1965 demonstrating the spatial resolution of the two-frame 6.151 keV backlighter. (a) Radially stretched radiograph image of the edge of the liner showing the machined sinusoidal perturbations. (b) Lineout through the radiograph image at the position indicated by the red bars demonstrating a 10%–90% edge-spread width of about 15 μm.

bubbles by the spikes in the smallest-wavelength modes. The timing of the radiographs with respect to the current is shown in Fig. 3. The radiographs have a spatial resolution of about 15 μm, as demonstrated in Fig. 4. The magnification of each radiograph varies slightly (a few percent) from shot to shot and from frame to frame. The magnification of each radiograph was estimated based on the axial wavelengths of the seeded region to within an estimated error of 2–3%. The importance of the magnification error is that the radial position of the liner edge that is inferred is uncertain by the same factor, which amounts to about ± 50 μm uncertainty in the absolute radius for values near 3 mm.

The third set of experiments used beryllium liners instead of Al liners. The same two-frame 6.151 keV backlighter was used as in the first set of Al experiments. The lower opacity at 6.151 keV of Be (2.24 cm^2/g) versus Al (102.6 cm^2/g) allows an in-flight measurement of the areal density, since the x-ray transmission through all parts of the liner exceeds 5% for most of the implosion. These experiments collected information on the growth of the MRT instability starting from initially flat contours (i.e., no sinusoidal perturbations).

The liner "targets" were manufactured by General Atomics using single-point diamond-turning machines in order to obtain the highest-quality surface finish possible. The resulting liners were characterized with a combination of high-resolution x-ray imaging using a commercial tunable bremsstrahlung x-ray source to produce 40–150 keV x rays and high-resolution optical light microscope interferometry. The x-ray imaging is used to measure the liner thickness and uniformity to within ± 2 μm. The optical interferometry provides information about the surface texture and roughness. The process for making these targets is still being refined at this time, but some improvements in Al and Be targets have already been realized since these experiments were done.

Example preshot characterization radiographs taken with the x-ray imaging system are shown in Fig. 5. The Al radiographs show no structure in the bulk material and the average wall thickness of the five targets from the first set of experiments was 273 μm, very close to the specified value of 272 μm. The Be radiographs show some speckle structure in the bulk material that is likely from grain structures. Some

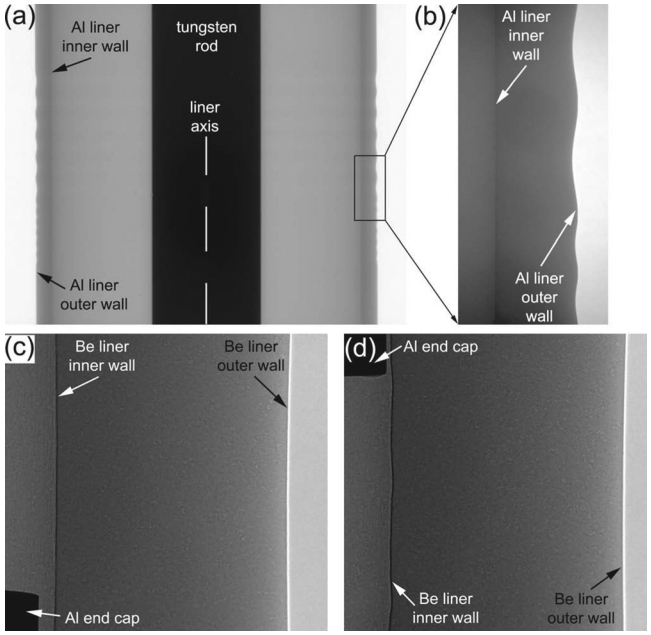

FIG. 5. Example x-ray characterization radiographs of Al and Be targets. (a) Whole body 85 keV Al target radiograph (series 1) showing the 2 mm diameter W rod on axis. (b) High-magnification view of the liner wall showing the machined perturbations. (c) Magnified 65 keV image of a uniform-thickness section of a Be target. (d) Magnified view of the same Be target in a region with thickness variations.

portions of the Be target had radius variations on the inner wall of about 6 μm in amplitude over a roughly 160 μm height. The wall thickness measurements averaged about 813 μm, slightly higher than the desired 800 μm.

Example unfiltered surface characterization data obtained from Al and Be targets are shown in Fig. 6. As shown

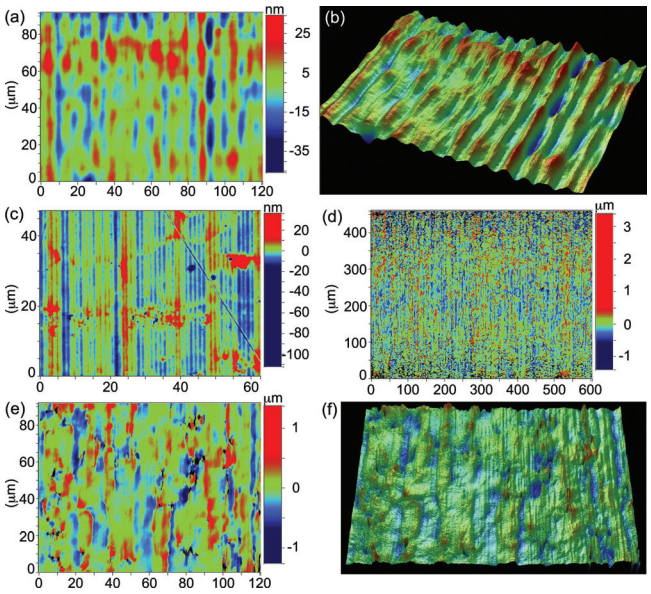

FIG. 6. (Color) Example surface profile data from Al and Be targets. (a) Contour plot of Al surface profile. (b) 3D version of the same data. (c) Higher-resolution image of Al surface profile (from a test piece), in which the expected 1.25 μm machining grooves are visible. (d) Contour plot of Be surface profile. (e) Higher-resolution image of Be surface profile. (f) 3D version of the same data. Note the change in contour plot amplitude units from nanometers to micrometers in going from Al to Be.

Downloaded 04 May 2011 to 198.102.153.2. Redistribution subject to AIP license or copyright; see http://pop.aip.org/about/rights_and_permissions

in Fig. 6(b) the surface roughness profile is not random, but has azimuthal striations caused by the spinning motion of the diamond-turning machine. The theoretical periodicity of this structure given the machine rotation rate and the tool feed rate is 1.25 μm. This periodicity can be seen in the highest-resolution image in Fig. 6(c). There is also another superimposed period of about 8 μm visible in the Al profiles of Figs. 6(a)–6(c), the origin of which is unknown. The root-mean-square surface roughness at the high magnification shown in Fig. 6(c) is in the 6–10 nm range. Over $5\times$ larger spatial scales the surface roughness of these Al targets increases to about 50–60 nm due to larger-scale nonuniformities in the radius. The Be surface profiles are distinctly different than the Al profiles in that they have larger amplitude variations and in that the roughness is not dominated nearly as much by the azimuthal striations. At all spatial scales shown in Figs. 6(d)–6(f) the root-mean-square surface roughness is about 210–240 nm.

III. EXPERIMENTAL DATA

The first experimental series studied Al tube liners in which 200- and 400 μm wavelength sinusoidal perturbations had been machined. These wavelength values were chosen to match LASNEX simulations of liners such as those shown in Fig. 1 from Ref. 6. The characteristic axial wavelength in those simulations when the liners approach the axis is roughly 200–400 μm. These wavelengths are also well-resolved by the 15 μm spatial resolution of the 6.151 keV backlighter demonstrated in Fig. 4, so we were confident that we would be able to observe the growth of the MRT instability in these first experiments. Additionally, the LASNEX simulations predicted dense plasma jets would be formed from ablated material when wavelengths of $\leq$200 μm were used and we wished to test that prediction.

The experimental radiograph data obtained during the first experimental series studying Al tube liners are summarized in Fig. 7. The eight frames of data were collected on five shots (z1962–z1965, z1968) using the two-frame radiography diagnostic (two frames of data were lost). As can be seen in Fig. 7(b), the left and right sides of the image show only small variations from one wave to another. This implies that the perturbations still remain highly correlated along the azimuth of the liner.

Several features can be seen in the radiograph sequence of Fig. 7(c). First, early in time the current diffuses into the liner and heats up its outermost layer. This layer becomes a plasma and ablates outward along a vector largely normal to the liner surface, so that the ablated plasma is focused by the sinusoidal curvature. In the higher-curvature 200 μm waves the focusing results in an early reversal of the apparent position of the peaks and valleys that eventually culminates in the distinct, narrow jets seen in the z1963a frame. Eventually the material in the jets diffuses to a low enough areal density to be invisible to the 6.151 keV x rays and/or is compressed back onto the liner by the increasing magnetic pressure. The plasma temperature in the jets (e.g., in the z1963a frame) is estimated in LASNEX simulations to be about 30 eV, and in the valleys about 100 eV. The amount of mass in the jets is relatively small (a few micrograms, equivalent to an $\sim$0.5 μm-thick layer of solid Al). By contrast, in the 400 μm data the peak-to-valley amplitude decreases to 17 μm in frame 1 (z1968a) due to ablation but thereafter the amplitude of the perturbation grows continuously without prominent jet formation.

A second series studied the development of the MRT instability in both flat regions (perturbed only by surface roughness) and regions with 25-, 50-, 100-, and 200 μm seeded perturbations. A single-frame 6.151 keV diagnostic was used to provide a horizontal (0°) view to prevent shadowing of the bubbles by the spikes in the smallest-wavelength modes. Radiographs were obtained on two experiments at $t=47.8$ and 75.4 ns in the current pulse (Fig. 3). The data are shown in Fig. 8. Expanded views of the 75.4 ns data are shown in Fig. 9. As with the first experimental series, the $\lambda=200$ μm features produced prominent jet structures, as did the smaller wavelength features. The engineered perturbation regions shown in Fig. 9(b) appear to be highly correlated along the azimuthal direction, though some deviations are visible at the smallest wavelengths and in the jet seen at $z=3.1$ mm. By contrast, the left and right images from the region of the liner without engineered perturbations [Fig. 9(c)] show significant differences. This means that the initial surface roughness variations of the liner in this region have given rise to instability structures that are not strictly two-dimensional (azimuthally correlated), but are three-dimensional in nature. It is important to note that some degree of azimuthal correlation exists, since a bubble penetrating from $r=2.9$ mm down to $r=2.8$ mm in the image traverses a chord with a length of about 1.5 mm covering about 15°of the liner's azimuthal extent. The unperturbed regions in the 47.8 and 75.4 ns radiographs had characteristic wavelengths of 65 and 120 μm and characteristic amplitudes of 3.2 and 70 μm, respectively. The 3.2 μm amplitude variation over a height of 65 μm is certainly pushing the limits of our 15 μm backlighter spatial resolution and it should be considered to have a large error bar.

A third series studied the development of the MRT instability in a beryllium liner instead of an aluminum liner. As noted earlier, the opacity of Be at 6.151 keV allows a significant fraction of the x rays to penetrate through all portions of the liner. This experiment was a proof-of-principle test intended to demonstrate that it was possible to make an in-flight areal density measurement. Two experiments were attempted, but timing problems with the Z-Beamlet backlighter resulted in only one pair of usable images, which is shown in Fig. 10. As seen in Fig. 10(c), the minimum transmission through the liner is 10% along the chords through the tubelike liner passing closest to the inside surface of the liner. A 2 mm diameter tungsten rod was used on the axis of the liner, as in the Al experiments. To provide an unobstructed view of the liner edges, the eight posts in the return-current can were supposed to be aligned so that two of the eight posts lined up with the liner axis. In the radiographs shown in Fig. 10, the opaque region on the axis is actually defined by the edges of the return-current posts, not the on-axis rod. Each post, which nominally carries 1/8 the total current, undergoes its own instability development that creates the ragged edges

Downloaded 04 May 2011 to 198.102.153.2. Redistribution subject to AIP license or copyright; see http://pop.aip.org/about/rights_and_permissions

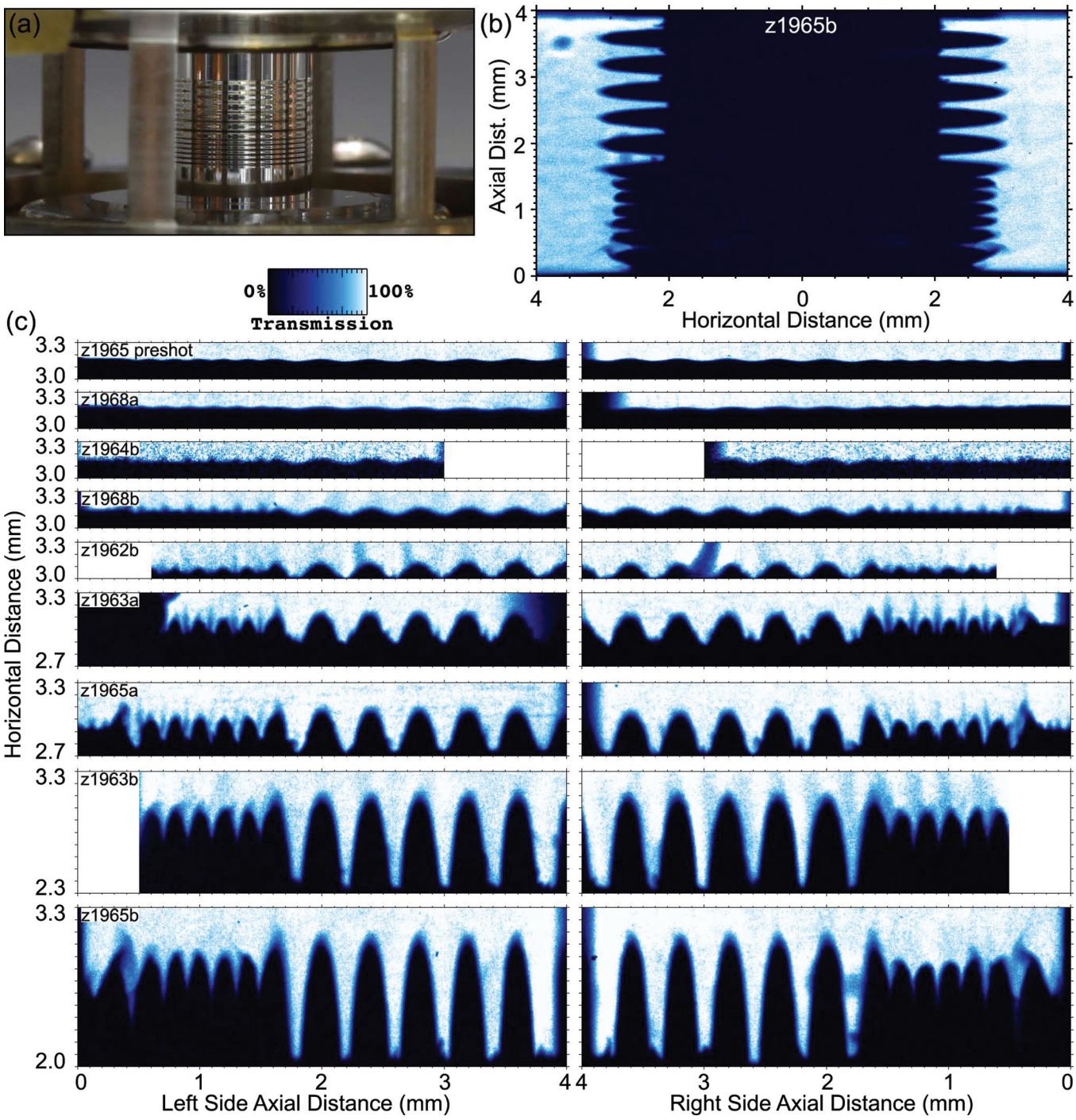

FIG. 7. (Color) Al liner data obtained during series 1. (a) Optical photo of the liner target installed in Z. (b) 6.151 keV radiograph of the central 4 mm height of the liner target. Six $\lambda = 400$ μm perturbations range from 1.6 to 4 mm axially and six $\lambda = 200$ μm perturbations range from 0.4 to 1.6 mm axially. The axial region from 0 to 0.4 mm was unperturbed. (c) Expanded views of the two liner edges from a preshot radiograph and eight frames taken during the current pulse (Fig. 3) at 30.5, 42.7, 45.8, 57.0, 63.6, 67.7, 79.0, and 83.0 ns, respectively. The radiographs have been cropped and rotated so that the z-axis is horizontal.

seen near ± 1 mm in the radiographs. The fact that the opaque edges seen are from the post rather than the on-axis rod is supported by the asymmetry of the edges with respect to the liner—the edges are shifted slightly to the left of center, whereas preshot 60 keV characterization radiographs showed the on-axis rod to be perfectly centered.

A careful look at the radiograph in Fig. 10(b) reveals that the instability perturbations on the left and right sides do not line up well, so that the level of azimuthal correlation is low. This is consistent with the radiography data shown for Al liners in Fig. 9(c). The transmission as a function of horizontal distance shown in Fig. 10(c), averaged over the entire vertical height of the image, is by contrast highly symmetric. The dashed lines show this average lineout flipped about the zero axis. The close overlay of the dashed and solid lines indicates a high degree of azimuthal symmetry in the average position and thickness of the liner. (The portions that do not match well are due to the return-current posts.)

Downloaded 04 May 2011 to 198.102.153.2. Redistribution subject to AIP license or copyright; see http://pop.aip.org/about/rights_and_permissions

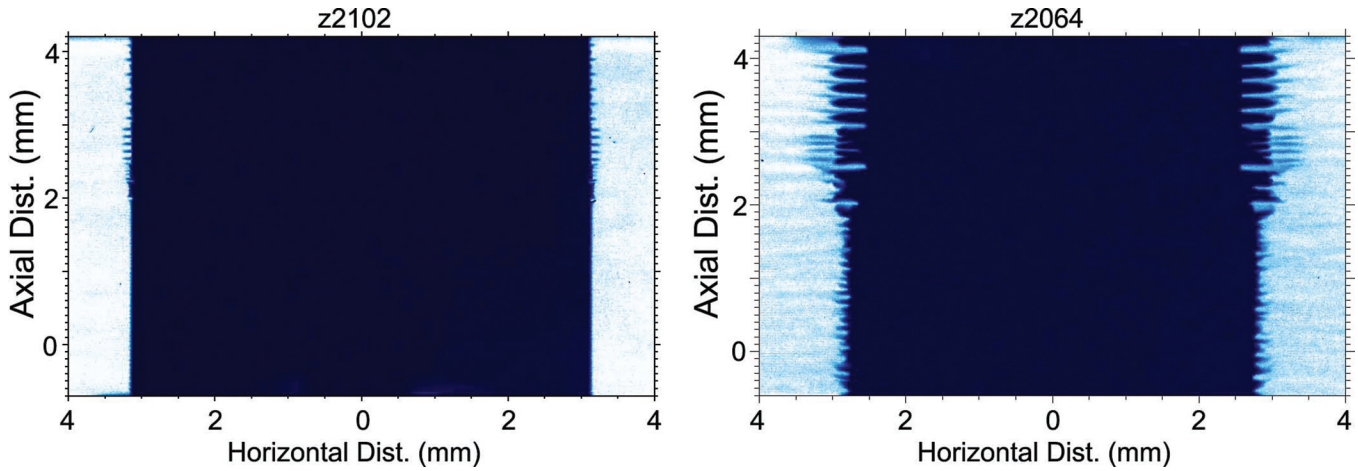

FIG. 8. (Color) Al liner data obtained during series 2 using the single-frame 6.151 keV backlighter. The MRT instability was seeded in the upper half of the targets (2–4.2 mm) with various sinusoidal perturbations. The rest of the target was machined as smooth as possible. (a) Full radiograph image from z2102 ($t = 47.8$ ns), taken when the ablation jets were well-defined. (b) Full radiograph image from z2064 ($t = 75.4$ ns), taken at a later time in the implosion.

IV. DISCUSSION

A plot of the peak-to-valley MRT instability amplitude versus time for the $\lambda = 400$ μm data is shown in Fig. 11. We estimate an error in the cross timing between the radiograph times and the measured current at ± 1.0 ns. The error in the amplitude is dominated by the shot-to-shot uncertainty in the magnification of about $\pm 3\%$ and the statistical variation in the amplitude from one feature to another, for a total uncertainty of about $\pm 5\%$. Also plotted is the amplitude of simulated radiographs of four-wave 2D LASNEX calculations. The simulations used a uniform density with an initial surface roughness that approximated the measured surface roughness of the Al. The simulations capture the overall trend and late-time amplitudes remarkably well, though they appear to underpredict the early-time amplitude growth.

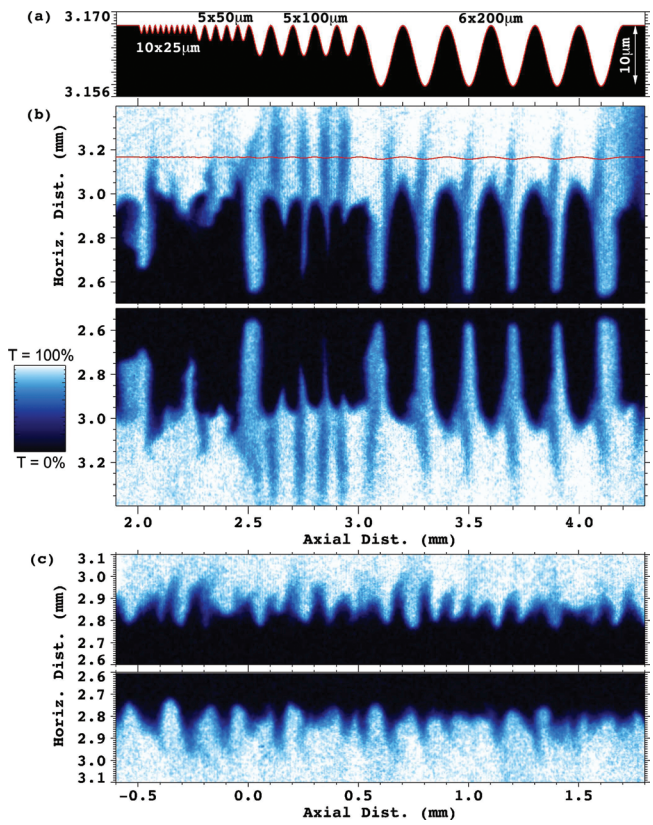

FIG. 9. (Color) Expanded views of the z2064 radiograph data shown in Fig. 8. The images shown have been cropped and rotated so that the z-axis is horizontal. (a) Diagram illustrating the position and amplitudes of the sinusoidal perturbations applied to the 2–4.2 mm region of the target. Note the distorted vertical scale. (b) Left and right side radiograph images of the perturbed region of the target. A red line shows the initial liner contour from part (a) on the scale of the image. (c) Left and right side radiograph images of the unperturbed region of the target. Note the decreased azimuthal symmetry relative to (b).

We compare these results to analytic theory for the growth of the magneto-Rayleigh–Taylor instability. The linearized equations describing the growth of the MRT instability amplitude can be described by two second-order differential equations (Eqs. 53 and 54 of Ref. 2), with a total of four solutions (one exponentially growing, one exponentially decaying, and two oscillatory solutions). Rearranging these equations, we can derive an equation for the exponentially growing and decreasing solutions,

$$\frac{d^2\eta}{dt^2} = \gamma^2(t)\eta, \tag{1}$$

where η is the amplitude and $\gamma^2 = kg(t)$ (k is the wavenumber of the perturbations given by $2\pi/\lambda$). In our original publication[1] we compared the experimental amplitude growth against only the exponentially growing solution of Eq. (1), which was estimated as $\eta = \eta_0 \exp[G(t)]$, where $G(t) = \int_0^t \gamma(t')dt'$. The decaying exponential term does become negligible but at early times it nearly cancels out the amplitude growth from the positive root. Thus, our original publication overestimated the amplitude growth predicted by theory. It would be more accurate to use the first-order WKB approximate solution of Eq. (1) with the initial conditions $\eta(t=0) = \eta_0$ and $d\eta/dt(t=0) = 0$, where η_0 is the initial peak-to-valley amplitude of the sinusoidal perturbation, which is $\eta = \eta_0 \cosh[G(t)]$. It is also possible to numerically integrate Eq. (1) with the same initial conditions. We did this, calculating the acceleration $g(t)$ from Newton's second law to be

Downloaded 04 May 2011 to 198.102.153.2. Redistribution subject to AIP license or copyright; see http://pop.aip.org/about/rights_and_permissions

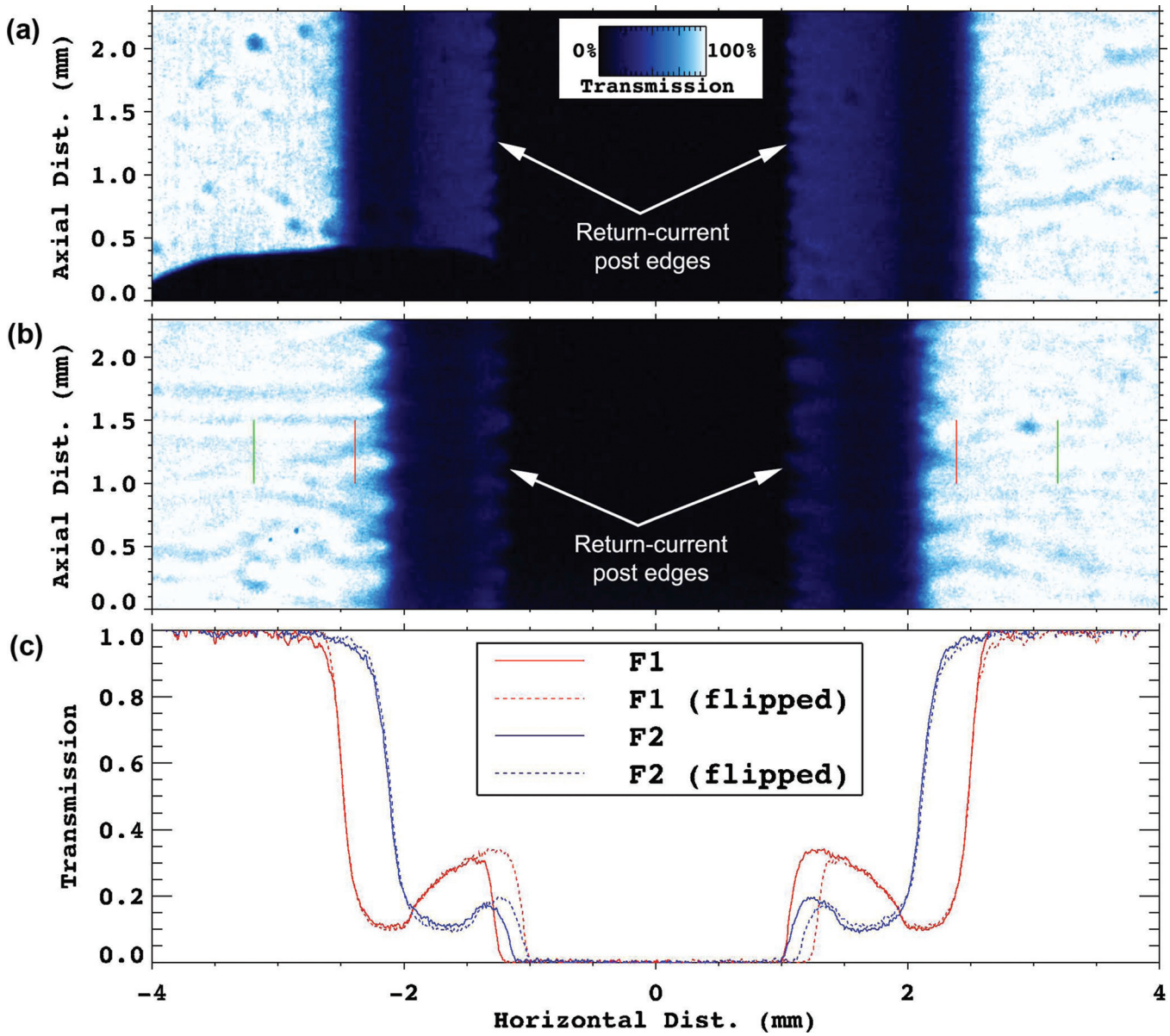

FIG. 10. (Color) Beryllium liner data obtained during shot z2060 of series 3. (a) Radiograph image taken at $t = 90.4$ ns. (b) Radiograph image taken at $t = 105.4$ ns. The initial liner outer and inner radii are indicated by the vertical green and red bars, respectively. (c) Horizontal lineout through the radiographs showing the average transmission as a function of horizontal distance. To indicate the symmetry of the data, the transmission lines were flipped about the zero axis and replotted as dashed lines. Note that the opaque region on the axis of the radiographs is caused by two of the eight return-current posts surrounding the load, not the on-axis tungsten rod.

$$g = -\frac{\mu_0}{4\pi m_L}\frac{I^2(t)}{R(t)}, \tag{2}$$

where m_L is the initial mass per unit length given by $2\pi R_0 \Delta r_0 \rho_0 = 0.158$ g/cm. The resulting solutions for the amplitude growth are plotted in Fig. 11.

The original publication[1] compared the data against the growing exponential solution, which clearly overestimates the amplitude growth. By contrast, the direct integral solution of the amplitude dispersion equation agrees much better with the LASNEX calculations and experimental data. The analytic solutions are not exact because as expressed here we are applying the acceleration to the entire liner thickness. In fact, in our LASNEX calculations it takes about 35 ns (until about 11 MA in the current pulse) before the shock in the liner reaches the inside liner surface, so before that time the actual mass per unit length being affected by the magnetic pressure is lower. Additionally, the calculations use as input the current and radius, which have errors on them as noted earlier. Finally, there is the obvious point that the analytic theory does not capture the early ablation and jet formation seen in the experiments. In the $\lambda = 400$ μm case, this results in a decrease in the amplitude as seen in Fig. 11, and for the smaller wavelengths the peaks and valleys reverse early in time. For this reason, we have not attempted to compare the analytic theory to the smaller wavelengths studied here. Nonetheless, we see that the analytic theory does appear to describe the general evolution of the instabilities seen in the data.

In our previous publication[1] we showed a number of detailed comparisons between the experimental radiographs

Downloaded 04 May 2011 to 198.102.153.2. Redistribution subject to AIP license or copyright; see http://pop.aip.org/about/rights_and_permissions

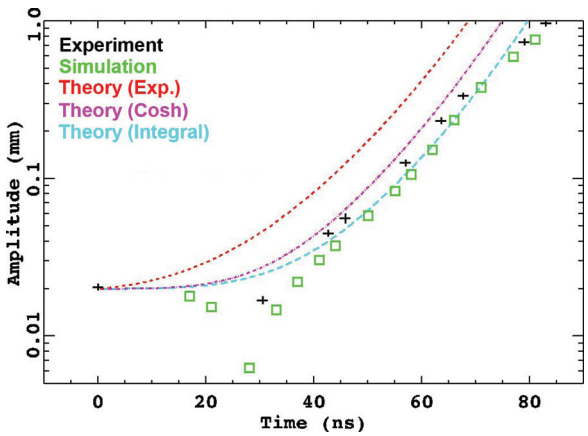

FIG. 11. (Color) Analysis of the $\lambda = 400$ μm data from series 1. The peak-to-valley amplitude vs time measured from the experiments is plotted as black crosses, where the extent of the crosses represents the measurement error. The green squares are the equivalent from LASNEX simulations. The dashed lines are various solutions to Eq. (1) obtained using a growing exponential approximation (red), a cosh function approximation (magenta), or a direct integration of the equation (cyan) as discussed in the text.

and results from 2D LASNEX calculations. These calculations, which are not reproduced in this paper due to space constraints, demonstrated remarkably good agreement with the experiments down to feature scales of about 50 μm. At the time of that publication, attempts had been made to simulate the experiments using both HYDRA[14] and GORGON,[15] both of which are newer radiation magnetohydrodynamic simulation codes capable of fully three-dimensional calculations. Those initial attempts were unsuccessful in capturing many of the important features of the data. Since that time we have continued to make progress in understanding the necessary physics to capture in our simulations. The remainder of this paper focuses on comparisons to 3D GORGON simulations that demonstrate our progress in modeling the MRT instability.

Simulations using the three-dimensional code GORGON were run to generate the simulated radiographs shown in Fig. 12, which appear to capture most of the key features of the experimental data. The simulations used an Eulerian mesh with a 0.67 μm radial, and 2 μm axial grid resolution. Only one cell in the azimuthal direction was modeled, making this effectively a two-dimensional simulation. With this fixed grid it is not possible to directly conform the mesh to the shape of the perturbed liner surface. Computational cells falling completely within the inner and outer liner radii were set to solid density. In regions where the outer boundary of

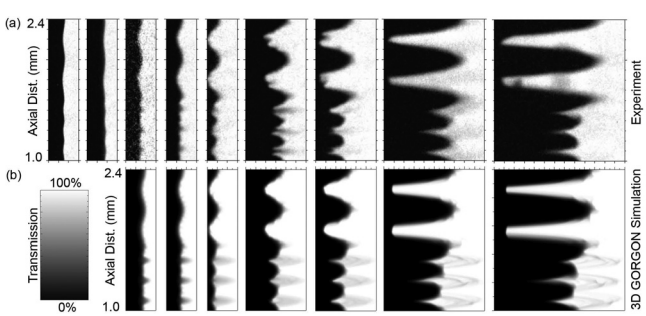

FIG. 12. Comparison of experimental radiographs of Al liners from series 1 (Fig. 7) and simulated radiographs calculated from a 3D GORGON simulation.

the liner bisected a computational zone, the correct mass was distributed over the entire zone. The original attempts at simulating the data used an ideal gas law equation of state for the aluminum, which was sufficient for modeling wire-array implosions.[16] This led to a number of unphysical effects in the high-density, low-temperature liner material, which were corrected in these simulations by the use of SESAME equation of state data tables[21] and Lee–Moore–Desjarlais electrical and thermal conductivities[22,23] for Al. Another change was that the original simulations used random density perturbations throughout the volume of the liner, while the newer calculations only perturb the mass in the outermost cells. The mass perturbation is equivalent to a random 100 nm peak amplitude, cell by cell variation in the liner outer radius to simulate the seeding of instabilities from surface roughness. As with our LASNEX calculations, it appears to be necessary to use a relatively high number of axial zones ($\geq$20 per wavelength) to capture the evolution of the instabilities. The simulations were driven by an applied current (i.e., not a circuit model), using the measured current from the experiments.

Subsequent Be liner comparisons in GORGON used the same code and methodology as the Al calculations, except that the full liner circumference was captured. A uniform three-dimensional Cartesian grid was employed with 20 μm cell sizes. The initial liner surface was perturbed by a 20 μm random surface roughness, so that the surface roughness was essentially applied at the grid resolution. At the relatively early times captured by the radiographs in Fig. 10, the MRT instability growth has had only a minor effect on the axial mass distributions. The radiographs in Fig. 10 were Abel-inverted to provide an axially averaged radial density profile, shown in Fig. 13. Corresponding density profiles from the 3D GORGON calculations are also overlaid. (Calculations with only one or two dimensions were also done, but because of the relatively small MRT growth at this time they give essentially the same profiles.) The GORGON profiles shown are actually both 0.9 ns later than the experimental radiograph times of 90.4 and 105.4 ns, respectively, but this difference is within the ± 1 ns error bar of the experimental timing (as well as the $\pm 3\%$ error of the current).

Comparisons of 2D and azimuthally resolved wedge calculations, to study the differences that geometry introduces in the growth of randomly seeded MRT instabilities, are the subject of ongoing work. A primary motivation for this is the observation that the unperturbed regions of the liner exhibit three-dimensional structure [e.g., Fig. 9(c)] that will not be adequately modeled by 2D LASNEX calculations. While the agreement between LASNEX and the data remains quite good in the perturbed regions and it is reasonably close in the unperturbed regions, the data shown here are from relatively low convergence ratios ($R_0/R_{\text{final}} \leq 1.5$) and we expect the agreement with 2D calculations to be increasingly poor as the liner approaches the axis.

Our primary objective with regard to achieving fusion in the laboratory is to assess the integrity of the inside liner surface at small radii. In future experiments we are planning to eliminate the on-axis rod and replace the eight posts in the return-current can with a solid Be wall. This will provide a clear view of the axis and it will eliminate azimuthal

Downloaded 04 May 2011 to 198.102.153.2. Redistribution subject to AIP license or copyright; see http://pop.aip.org/about/rights_and_permissions

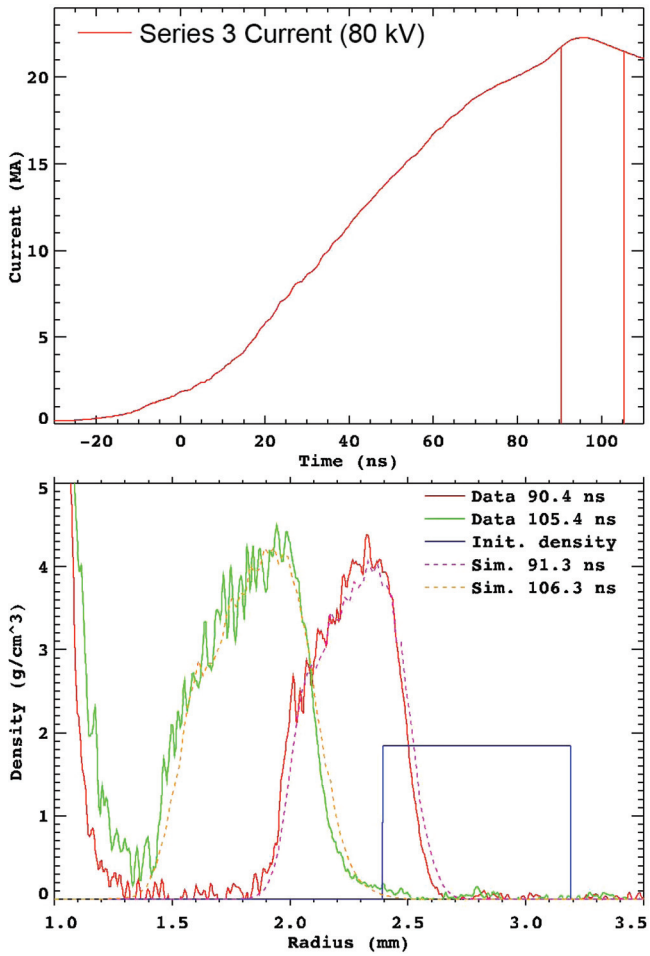

FIG. 13. (Color) Analysis of Be liner radiographs from series 3. The top plot indicates when the radiographs were taken relative to the current. The bottom plot compares the radial density profiles inferred from an Abel inversion of the data in Fig. 10 with profiles from 3D GORGON simulations. The initial density is also shown for comparison.

magnetic field perturbations resulting from the posts. Combined with the use of beryllium liners, we should be able to better determine the level of azimuthal correlation in the liner and whether it breaks apart before reaching the axis.

V. SUMMARY

We have presented substantially new and high quality experimental data on the growth of the magneto-Rayeigh–Taylor instability in ~100-ns Z-pinch implosions. At early times we observe the ablation of the outermost layer of the liner due to resistive heating. The ablated mass is ejected nearly normal to the surface, so that in smaller wavelength perturbations the ablated mass forms readily visible jet structures. In the largest wavelength data studied ($\lambda = 400$ μm) this ablated mass initially decreases the amplitude of the perturbations but eventually the amplitude growth due to the MRT instability is similar to that predicted from theory. These general features have been reproduced in some of the available radiation-magnetohydrodynamic simulation tools. Indeed, we have found excellent quantitative agreement as demonstrated for 2D LASNEX in our original publication[1] and here for 3D GORGON calculations. The data are providing us with insight into the important physics that needs to be modeled (e.g., use of the proper equation of state for Al, surface perturbations instead of volume density perturbations, etc.).

The success of the LASNEX modeling is encouraging because the simulations used the same methodology that was previously used to design a magnetized liner inertial fusion target for the Z facility.[6] Those designs appear to be capable of producing ≥100 kJ yields. Since the fusion fuel in those simulations absorbs roughly 100–200 kJ, this would mean that we may be able to get as much energy out as we put into the fusion fuel. This "scientific breakeven" has not yet been achieved in the laboratory. A major threat to the success of that concept is the magneto-Rayleigh–Taylor instability. Designs capable of ≥100 kJ yields mitigated this threat by using liners with outer radius to thickness ratios of 4–6. The MRT instability growing on the outside surface then only minimally perturbs the inside liner surface, as shown in Fig. 1. The success of LASNEX in modeling this MRT data increases the credibility of those predictions and increases our optimism about the feasibility of this concept. We are in the process of confirming the 2D LASNEX predictions using 3D simulation tools such as GORGON and HYDRA. The data contained here have been critical to that effort.

ACKNOWLEDGMENTS

We thank the Z, Z-Beamlet, diagnostics, target, and hardware teams for their support of this work, which was partially funded by Laboratory Directed Research and Development funds at Sandia. Sandia is a multiprogram laboratory operated by Sandia Corporation, a Lockheed Martin Company, for the National Nuclear Security Administration under DE-AC04-94AL85000.

[1]D. B. Sinars, S. A. Slutz, M. C. Herrmann, R. D. McBride, M. E. Cuneo, K. J. Peterson, R. A. Vesey, C. Nakhleh, B. E. Blue, K. Killebrew, D. Schroen, K. Tomlinson, A. D. Edens, M. R. Lopez, I. C. Smith, J. Shores, V. Bigman, G. R. Bennett, B. W. Atherton, M. Savage, W. A. Stygar, G. T. Leifeste, and J. L. Porter, Phys. Rev. Lett. **105**, 185001 (2010).
[2]E. G. Harris, Phys. Fluids **5**, 1057 (1962).
[3]E. Ott, Phys. Rev. Lett. **29**, 1429 (1972).
[4]D. D. Ryutov, M. S. Derzon, and M. K. Matzen, Rev. Mod. Phys. **72**, 167 (2000).
[5]A. R. Miles, Phys. Plasmas **16**, 032702 (2009).
[6]S. A. Slutz, M. C. Herrmann, R. A. Vesey, A. B. Sefkow, D. B. Sinars, D. C. Rovang, K. J. Peterson, and M. E. Cuneo, Phys. Plasmas **17**, 056303 (2010).
[7]T. J. Nash, D. H. McDaniel, R. J. Leeper, C. D. Deeney, T. W. L. Sanford, K. Struve, and J. S. DeGroot, Phys. Plasmas **12**, 052705 (2005).
[8]B. Jones, C. Deeney, J. L. McKenney, C. J. Garasi, T. A. Mehlhorn, A. C. Robinson, S. E. Wunsch, S. N. Bland, S. V. Lebedev, J. P. Chittenden, S. C. Bott, D. J. Ampleford, J. B. A. Palmer, J. Rapley, G. N. Hall, and B. V. Oliver, Phys. Rev. Lett. **95**, 225001 (2005).
[9]S. V. Lebedev, F. N. Beg, S. N. Bland, J. P. Chittenden, A. E. Dangor, M. G. Haines, K. H. Kwek, S. A. Pikuz, and T. A. Shelkovenko, Phys. Plasmas **8**, 3734 (2001).
[10]M. E. Cuneo, E. M. Waisman, S. V. Lebedev, J. P. Chittenden, W. A. Stygar, G. A. Chandler, R. A. Vesey, E. P. Yu, T. J. Nash, D. E. Bliss, G. S. Sarkisov, T. C. Wagoner, G. R. Bennett, D. B. Sinars, J. L. Porter, W. W. Simpson, L. E. Ruggles, D. F. Wenger, C. J. Garasi, B. V. Oliver, R. A. Aragon, W. E. Fowler, M. C. Hettrick, G. C. Idzorek, D. Johnson, K. Keller, S. E. Lazier, J. S. McGurn, T. A. Mehlhorn, T. Moore, D. S. Nielsen, J. Pyle, S. Speas, K. W. Struve, and J. A. Torres, Phys. Rev. E **71**, 046406 (2005).

Downloaded 04 May 2011 to 198.102.153.2. Redistribution subject to AIP license or copyright; see http://pop.aip.org/about/rights_and_permissions

[11]D. B. Sinars, M. E. Cuneo, E. P. Yu, D. E. Bliss, T. J. Nash, J. L. Porter, C. Deeney, M. G. Mazarakis, G. S. Sarkisov, and D. F. Wenger, Phys. Rev. Lett. **93**, 145002 (2004).
[12]R. E. Reinovsky, W. E. Anderson, W. L. Atchison, C. E. Ekdahl, R. J. Faehl, I. R. Lindemuth, D. V. Morgan, M. Murillo, J. L. Stokes, and J. S. Shlachter, IEEE Trans. Plasma Sci. **30**, 1764 (2002).
[13]G. B. Zimmerman and W. L. Kruer, Comments Plasma Phys. Control. Fusion **2**, 51 (1975).
[14]M. M. Marinak, G. D. Kerbel, N. A. Gentile, O. Jones, D. Munro, S. Pollaine, T. R. Dittrich, and S. W. Haan, Phys. Plasmas **8**, 2275 (2001).
[15]J. P. Chittenden, S. V. Lebedev, C. A. Jennings, S. N. Bland, and A. Ciardi, Plasma Phys. Control. Fusion **46**, B457 (2004).
[16]C. A. Jennings, M. E. Cuneo, E. M. Waisman, D. B. Sinars, D. J. Ampleford, G. R. Bennett, W. A. Stygar, and J. P. Chittenden, Phys. Plasmas **17**, 092703 (2010).
[17]E. M. Waisman and M. E. Cuneo, Phys. Rev. ST Accel. Beams **12**, 090401 (2009).
[18]T. C. Wagoner, W. A. Stygar, H. C. Ives, T. L. Gilliland, R. B. Spielman, M. F. Johnson, P. G. Reynolds, J. K. Moore, R. L. Mourning, D. L. Fehl, K. E. Androlewicz, J. E. Bailey, R. S. Broyles, T. A. Dinwoodie, G. L. Donovan, M. E. Dudley, K. D. Hahn, A. A. Kim, J. R. Lee, R. J. Leeper, G. T. Leifeste, J. A. Melville, J. A. Mills, L. P. Mix, W. B. S. Moore, B. P. Peyton, J. L. Porter, G. A. Rochau, G. E. Rochau, M. E. Savage, J. F. Seamen, J. D. Serrano, A. W. Sharpe, R. W. Shoup, J. S. Slopek, C. S. Speas, K. W. Struve, D. M. V. D. Valde, and R. M. Woodring, Phys. Rev. ST Accel. Beams **11**, 100401 (2008).
[19]G. R. Bennett, I. C. Smith, J. E. Shores, D. B. Sinars, G. Robertson, B. W. Atherton, M. C. Jones, and J. L. Porter, Rev. Sci. Instrum. **79**, 10E914 (2008).
[20]D. B. Sinars, G. R. Bennett, D. F. Wenger, M. E. Cuneo, D. L. Hanson, J. L. Porter, R. G. Adams, P. K. Rambo, D. C. Rovang, and I. C. Smith, Rev. Sci. Instrum. **75**, 3672 (2004).
[21]G. I. Kerley, Int. J. Impact Eng. **5**, 441 (1987).
[22]Y. T. Lee and R. M. Moore, Phys. Fluids **27**, 1273 (1984).
[23]M. P. Desjarlais, Contrib. Plasma Phys. **41**, 267 (2001).

Downloaded 04 May 2011 to 198.102.153.2. Redistribution subject to AIP license or copyright; see http://pop.aip.org/about/rights_and_permissions